CONSTRAINTS ON THE LIFETIMES OF DISKS RESULTING FROM TIDALLY DESTROYED ROCKY PLANETARY BODIES

J. GIRVEN[1], C. S. BRINKWORTH[2,3], J. FARIHI[4], B. T. GÄNSICKE[1], D. W. HOARD[2], T. R. MARSH[1], AND D. KOESTER[5]

[1] Department of Physics, University of Warwick, Coventry CV4 7AL, UK; j.m.girven@warwick.ac.uk
[2] *Spitzer* Science Center, California Institute of Technology, Pasadena, CA 91125, USA
[3] NASA Exoplanet Science Institute, California Institute of Technology, Pasadena, CA 91125, USA
[4] Department of Physics and Astronomy, University of Leicester, Leicester LE1 7RH, UK
[5] Institut für Theoretische Physik und Astrophysik, University of Kiel, 24098 Kiel, Germany

ABSTRACT

Spitzer IRAC observations of 15 metal-polluted white dwarfs reveal infrared excesses in the spectral energy distributions of HE 0110−5630, GD 61, and HE 1349−2305. All three of these stars have helium-dominated atmospheres, and their infrared emissions are consistent with warm dust produced by the tidal destruction of (minor) planetary bodies. This study brings the number of metal-polluted, helium and hydrogen atmosphere white dwarfs surveyed with IRAC to 53 and 38, respectively. It also nearly doubles the number of metal-polluted helium-rich white dwarfs found to have closely orbiting dust by *Spitzer*. From the increased statistics for both atmospheric types with circumstellar dust, we derive a typical disk lifetime of $\log[t_{\rm disk}({\rm yr})] = 5.6 \pm 1.1$ (ranging from 3×10^4 to 5×10^6 yr). This assumes a relatively constant rate of accretion over the timescale where dust persists, which is uncertain. We find that the fraction of highly metal-polluted helium-rich white dwarfs that have an infrared excess detected by *Spitzer* is only 23%, compared to 48% for metal-polluted hydrogen-rich white dwarfs, and we conclude from this difference that the typical lifetime of dusty disks is somewhat shorter than the diffusion timescales of helium-rich white dwarf. We also find evidence for higher time-averaged accretion rates onto helium-rich stars compared to the instantaneous accretion rates onto hydrogen-rich stars; this is an indication that our picture of evolved star–planetary system interactions is incomplete. We discuss some speculative scenarios that can explain the observations.

Key words: circumstellar matter – minor planets, asteroids: general – planetary systems – stars: abundances – white dwarfs

Online-only material: color figures

1. INTRODUCTION

Over the past decade it has become increasingly clear that planetary systems survive, at least in part, the late evolution of their host stars. The observational evidence supporting this conclusion comes from metal pollution observed in white dwarf atmospheres, and the commonly detected circumstellar disks of solid and gaseous debris (e.g., Zuckerman & Becklin 1987; Kilic et al. 2006; Gänsicke et al. 2006, 2007, 2008; Jura et al. 2007; von Hippel et al. 2007; Brinkworth et al. 2009; Farihi et al. 2010b, 2011; Debes et al. 2011; Melis et al. 2011; Brinkworth et al. 2012, and a host of other references therein).

Due to the high surface gravities and limited radiative forces, heavy elements sink rapidly within the atmospheres of cool ($T_{\rm eff} < 25,000$ K) white dwarf stars, resulting in essentially pure hydrogen or helium spectra (Koester 2009). The downward diffusion of metals occurs over a timescale that is typically only days to years for hydrogen-rich (DA type) atmospheres (above ∼11,000 K). Despite this, a notable fraction of cool DA white dwarfs exhibit absorption features due to the presence of trace metals (Zuckerman et al. 2003; Koester et al. 2005b), and these must be the result of external sources and a sign of ongoing accretion (Sion et al. 1990).

In numerous cases, the origin of these pollutants have been unambiguously identified as circumstellar dust, primarily via *Spitzer* studies (e.g., Reach et al. 2005; Jura et al. 2009; Farihi et al. 2009, 2010b). Gaseous disks components are detected around a number of stars, and the analysis of their dynamics demonstrates that the material is located within ∼1 $R_{\odot}$

(Gänsicke et al. 2006, 2007, 2008), where large solid bodies should be destroyed by tidal gravitational forces (Davidsson 1999). The chemical abundances of these photospheric pollutants can be analytically linked to those of the accreted matter (Koester 2009). In a number of cases, the closely orbiting dust has been confirmed to be silicate-rich, and typical of the material associated with planet formation (e.g., zodiacal and cometary dust; Reach et al. 2005; Jura et al. 2009; Reach et al. 2009). Studying planetary systems around white dwarfs therefore unlocks the potential to measure the bulk chemical composition of destroyed, and subsequently accreted, rocky planetary bodies such as asteroids, moons, or possibly major planets (e.g., Zuckerman et al. 2007; Dufour et al. 2010; Farihi et al. 2011; Klein et al. 2011).

The favored and successful model of a tidally destroyed asteroid (Graham et al. 1990; Jura 2003) is consistent with the observed disk properties (Gänsicke et al. 2006; Farihi et al. 2010a; Melis et al. 2011; Debes et al. 2011), the subsequent photospheric pollution, and the composition of both the orbiting and accreted material (e.g., Klein et al. 2011; Zuckerman et al. 2011). Such a catastrophic destruction is most readily achieved by a remnant planetary system with at least one major planet (Debes & Sigurdsson 2002) that perturbs a belt of smaller objects. Thus, white dwarfs with disks and photospheric metals may harbor complex planetary systems.

A significant uncertainty is the typical lifetime of the dust disks (Jura 2008; Kilic et al. 2008), yet this is an important indicator of the mass of the parent body (or bodies) that generated the observed debris. There are numerous stars with cooling ages

Table 1
Spitzer IRAC White Dwarf Targets

WD	Name	SpT	V (mag)	M ($M_\odot$)	$T_{\rm eff}$ (K)	$t_{\rm cool}$ (Gyr)	[H/He]	[Ca/H(e)]	$\log \langle dM_z/dt \rangle$ (g s^{-1})	$\log (M_z)$ (g)	Ref
0110−565	HE 0110−5630	DBAZ	15.9	0.71	19 200	0.12	−4.2	−7.9	8.4	20.2	1,2
0435+410	GD 61	DBAZ	14.9	0.72	17 300	0.20	−4.0	−7.5	8.9	21.5	3
0446−255	HE 0446−2531	DBAZ	16.8	0.59	12 600	0.36	−3.2	−5.7[a]	11.5	24.9	4
0449−259	HE 0449−2554	DBAZ	16.3	0.72	12 500	0.52	−4.5	−7.2[a]	10.0	23.5	4
0802+386	G111-54	DZ	15.5	0.78	11 000	0.85	<−6.0	−9.8	7.4	21.1	5
0838+375	CBS 78	DBZ	17.7	0.59	12 500	0.36	<−5.0	−8.0	9.2	22.7	6
0953+594	SDSS	DZA	18.4	0.58	8 200	1.12	−3.2	−7.5	9.7	23.6	5
1015+377	CBS 127	DZ	17.7	0.58	10 500	0.59	<−5.0	−8.2	9.1	22.8	6
1349−230	HE 1349−2305	DBAZ	16.5	0.67	18 200	0.14	−4.7	−8.0	8.7	22.0	1,2
1350−162	HE 1350−1612	DBAZ	17.0	0.77	15 000	0.35	−4.7	−6.7[a]	10.4	23.4	4
1352+004	PG	DBAZ	15.8	0.59	15 300	0.20	−4.8	−9.3	7.7	20.7	1
1614+160	PG	DAZ	15.6	0.50	17 400	0.10	. . .	−7.2	7.8	. . .	1
2138−332	NLTT 51844	DZ	14.5	0.69	7 200	2.23	. . .	−8.6	8.5	22.5	7
2142−169[b]	PHL 131	DO	15.8	. . .	. . .	. . .	. . .	. . .	. . .	. . .	2
2229+139	PG	DBAZ	16.0	0.83	15 900	0.36	−4.5	−9.0	8.0	20.9	1
2322+118	LB 1188	DZA	16.0	0.59	12 000	0.41	−5.2	−8.7	8.5	22.1	1

Notes. Objects found to have dust disks are listed in italics. The tenth column lists time-averaged metal in-fall rates. The eleventh column shows the mass of metals in the convective envelopes of the helium-rich stars. Both quantities are calculated based on the observed calcium abundances and assuming this represents 1.6% of the total mass of heavy elements, as in the bulk Earth (Allègre et al. 1995).
[a] Klein et al. (2011) find that HS 2253+8023 has a lower calcium abundance by around 1.0 dex than originally reported. This may therefore also be true of other Friedrich et al. (2000) stars.
[b] Not metal-rich.
References. (1) Koester et al. 2005a; (2) Voss et al. 2007; (3) Desharnais et al. 2008; (4) Friedrich et al. 2000; (5) Dufour et al. 2007; (6) Dupuis et al. 1993; (7) Subasavage et al. 2007.

greater than 1 Gyr that exhibit atmospheric metal pollution, such as the prototype vMa 2 (van Maanen 1917; Greenstein 1956; Weidemann 1960). Koester et al. (2011) recently identified 26 white dwarfs with temperatures 5000–8000 K and 10^{20}–10^{23} g of accreted metals in their convection zones. These stars have typical ($\log g = 8$) cooling ages of 1–6 Gyr but must have accreted material recently, within the past few million years. Interestingly, there is only a single (and anomalous) infrared excess around stars with cooling ages older than 1 Gyr (G166-58; Farihi et al. 2008), so this may be viewed as an upper limit for typical disk lifetimes.

From theoretical considerations, Rafikov (2011a) finds the lifetimes of the compact dust disks around white dwarfs should be on the order of 10^6 yr when dominated by Poynting–Robertson drag. However, Poynting–Robertson drag cannot produce the highest (average) accretion rates inferred for the helium atmosphere stars (DB) with metals, which are on the order of 10^{10}–10^{11} g s^{-1} (Farihi et al. 2010b). Xu & Jura (2012) extend the estimates of Rafikov (2011a) and find a factor of five higher accretion rates, but this still does not lead to high enough rates. To produce higher accretion rates, gas resulting from sublimated dust, produced at the inner edge of the dust disk (Jura 2008; Farihi et al. 2009), efficiently transports angular momentum outward and fuels a more rapid in-fall of material. Rafikov (2011b) calculates that the lifetime of a 10^{22} g disk is reduced to several 10^4 yr.

We report the results of a combined *Spitzer* IRAC Cycle 5 and 6 search for disks around 15 cool, metal-contaminated white dwarfs. Three of the observed stars show infrared excess that is the trademark of warm dust orbiting within the tidal disruption radius: HE 0110−5630, GD 61, and HE 1349−2305. These three stars significantly increase the number of metal-polluted DB white dwarfs with disks and enable a statistical estimate of a typical disk lifetime based on comparison with their

DA counterparts. The observations are described in Section 2, the analysis and disk modeling in Section 3. In Section 4 the statistics of dusty white dwarfs is revisited, and our method for estimating disk lifetimes is described.

2. OBSERVATIONS

We were awarded *Spitzer Space Telescope* time in Cycle 5 (program 50340) and Cycle 6 (program 60119), to search for infrared excesses from circumstellar dust around 16 white dwarfs published as metal-enriched (Table 1). These targets were chosen from the literature, and significantly increase the number of DBZ (for simplicity, we use "DBZ" to refer to all helium-rich subtypes with metals, including those with trace hydrogen) stars observed with *Spitzer* IRAC, bringing their numbers onto par with those of the DAZ stars. One of the targets, PHL 131, was subsequently found by one of us (D.K.) to be a 40,000 K white dwarf with interstellar calcium absorption, and thus we report its fluxes, but exclude it from the rest of the study.

Imaging observations were obtained for each of the white dwarf targets using the Infrared Array Camera (IRAC; Fazio et al. 2004). Exposures were taken in the 4.5 and 7.9 μm channels using the medium-scale, cycling dither pattern for the Cycle 5 targets objects and in the 3.6 and 4.5 μm channels for the Cycle 6 objects. For GD 61 and NLTT 51844, images were also obtained with the blue Peak-Up Imaging array of the Infrared Spectrograph at 15.6 μm, this time using the small-scale, cycling dither pattern.

Three of the target white dwarfs were chosen from the Hamburg Schmidt (HS; Hagen et al. 1995) and the Hamburg European Southern Observatory Schmidt (HE; Wisotzki et al. 1996) quasar surveys. As discussed in Farihi et al. (2010b), the SIMBAD coordinates for these objects are often inaccurate by up to a few arcminutes. Table 2 gives correct positions for these sources based on their IRAC images.

Table 2
IRAC Coordinates for HE and HS White Dwarfs

Star	α	δ
HE 0110−5630	$01^h12^m21^s15$	$-56°14'27''8$
HE 0446−2531	$04^h49^m01^s39$	$-25°26'36''1$
HE 0449−2554	$04^h51^m53^s72$	$-25°49'14''7$
HE 1349−2305	$13^h52^m44^s13$	$-23°20'05''4$
HE 1350−1612	$13^h53^m34^s96$	$-16°27'06''6$

Note. Epoch 2009 positions as measured on the IRAC array from image header astrometry.

2.1. Data Analysis

The IRAC image photometry was performed on the individual BCD frames downloaded from the *Spitzer* archive and reduced using S18.7.0. These were corrected for array-location dependence as described in the IRAC Data Handbook.[6] We used the point source extraction package APEX MULTIFRAME within MOPEX (Makovoz et al. 2006) to perform point-spread function (PSF) fitting photometry on the individual BCDs. We do not apply a color correction because we use the isophotal wavelengths in our analysis. The magnitude of the correction is therefore negligible compared to our uncertainties. The pixel phase correction for channel 1 data is also minimal in comparison to the uncertainties and therefore was not applied. A minimum 5% uncertainty on the flux density was assigned to account for the systematic uncertainties in this method (Reach et al. 2005).

The Infrared Spectrometer (IRS; Houck et al. 2004) Peak-up Imaging was analyzed according to the method of Brinkworth et al. (2012). The sky background was found to be variable over the array (see Figure 1), so the individual BCDs were initially median-combined to make both a flat and sky, using 3σ rejection. This was then scaled to the overall median of the post-BCD mosaic and subtracted from each of the individual BCDs. To completely reduce the sky level to zero, the edges of the image were temporarily discarded and a median of the center of the image was found and removed. The sky can therefore be assumed to be zero and an infinite sky annulus is effectively used during photometry. The flat-fielded and median-subtracted BCDs were mosaicked using MOPEX with a dual-outlier rejection. The pixel scale for the mosaic was set to the default $1''8$ pixel^{-1}. The photometry was performed with APPHOT within IRAF using a 3 pixel aperture radius, but no sky subtraction. The aperture correction to the calibration aperture sizes, as provided by the *Spitzer* Science Center, was performed and the fluxes were converted from MJy sr^{-1} to mJy. As an estimate of the error, a series of other apertures were placed around the target on the mosaic and the standard deviation of fluxes was taken as the uncertainty. All measured *Spitzer* fluxes are listed in Table 3.

2.2. Near-infrared Observations

Supplemental near-infrared photometry for most target stars was obtained on the 2011 March 23 with the William Herschel Telescope using the Long-Slit Intermediate Resolution Infrared Spectrograph (LIRIS; Manchado et al. 1998), and on 2011 August 10–12 with the New Technology Telescope using Son of Isaac (SOFI; Moorwood et al. 1998). Images taken in a nine-point dither pattern were obtained with the *J*, *H*, and *K*$_s$-band filters with typical total exposure times of 270 s in clear

Table 3
Spitzer IRAC and IRS Fluxes

WD	$F_{3.6\,\mu m}$ (μJy)	$F_{4.5\,\mu m}$ (μJy)	$F_{7.9\,\mu m}$ (μJy)	$F_{15.6\,\mu m}$ (μJy)
0110−565	135 ± 9	124 ± 8	. . .	. . .
0435+410	. . .	259 ± 13	153 ± 8	98 ± 10
0446−255	. . .	26 ± 1	15[a]	. . .
0449−259	. . .	39 ± 2	24 ± 1	. . .
0802+386	. . .	85 ± 4	38 ± 2	. . .
0838+375	18 ± 1	13 ± 1	. . .	. . .
0953+594	. . .	9 ± 1	6[a]	. . .
1015+377	20 ± 1	14 ± 1	. . .	. . .
1349−230	. . .	88 ± 2	66 ± 3	. . .
1350−162	. . .	23 ± 2	7[a]	. . .
	32 ± 2	23 ± 1	. . .	. . .
1352+004	. . .	52 ± 3	15 ± 2	. . .
1614+160	. . .	63 ± 3	32 ± 2	. . .
2138−332	. . .	503 ± 25	195 ± 10	95 ± 15
2142−169[b]	. . .	35 ± 2	12 ± 4	. . .
2229+139	. . .	43 ± 2	13 ± 2	. . .
2322+118	105 ± 5	69 ± 3	. . .	. . .

Notes. A 5% uncertainty has been folded in to account for calibration errors (Reach et al. 2005). Pipeline S18.7.0 was used to obtain BCD products for all targets.
[a] 3σ upper limit.
[b] Not metal-polluted.

conditions; three standard star fields were observed in a similar manner for photometric zero-point calibration. These data were reduced in the standard manner, by subtracting a median sky from each image in the dithered stack, flat fielding (using sky flats), then averaging and recombining frames.

LIRIS suffers from what is known as a detector reset anomaly, which appears in certain frames as a discontinuous jump (in dark current) between the upper and the lower two quadrants. To remove this unwanted signal, after flat fielding and sky subtraction, the detector rows were collapsed into a median column (with real sources rejected) and subsequently subtracted from the entire two dimensional image. The resulting fully reduced frames exhibit smooth backgrounds, free of the anomalous gradient. Analogously, SOFI exhibits significant cross-talk between quadrants, which becomes apparent for bright sources. The IRAF script CROSSTALK was employed on each of the raw frames prior to processing as described above, effectively removing any unwanted artifacts.

Aperture photometry of standard stars and relatively bright targets was performed using $r \approx 4''$ aperture radii and sky annuli of ranging between $5''$ and $8''$. For relatively faint targets or those with neighboring sources, smaller apertures were employed with corrections derived from several brighter stars within the same image field and filter. In a few cases, PSF-fitting photometry (i.e., DAOPHOT) was used as a second method in addition to photometry with small apertures. All data taken in the K_s-band filter were flux-calibrated using ARNICA (Hunt et al. 1998) *K*-band standard star photometry. The measured photometry can be found in Table 4.

3. ANALYSIS AND RESULTS

3.1. Removal of Nearby Background Source Flux

The IRAC mosaicked images of GD 61, CBS 127, and HE 1349−2305 all reveal nearby background objects that have the potential to contaminate aperture photometry (see
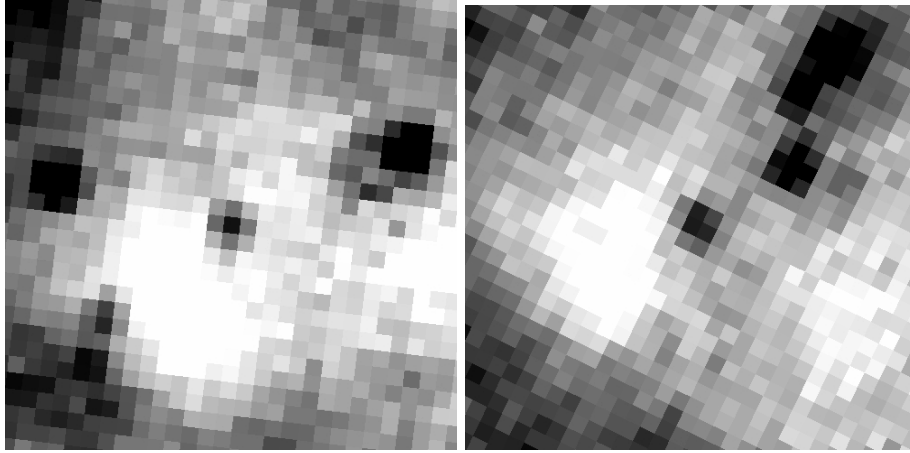
Figure 1. IRS Peak-Up image mosaics of GD 61 (left) and NLTT 51844 (right). The images are orientated north up and east left at $1\overset{''}{.}8$ pixel^{-1} and $50''$ across. The background is clearly variable across the array and is therefore the primary source of error (Section 2.1).

Table 4
Near-infrared Photometry

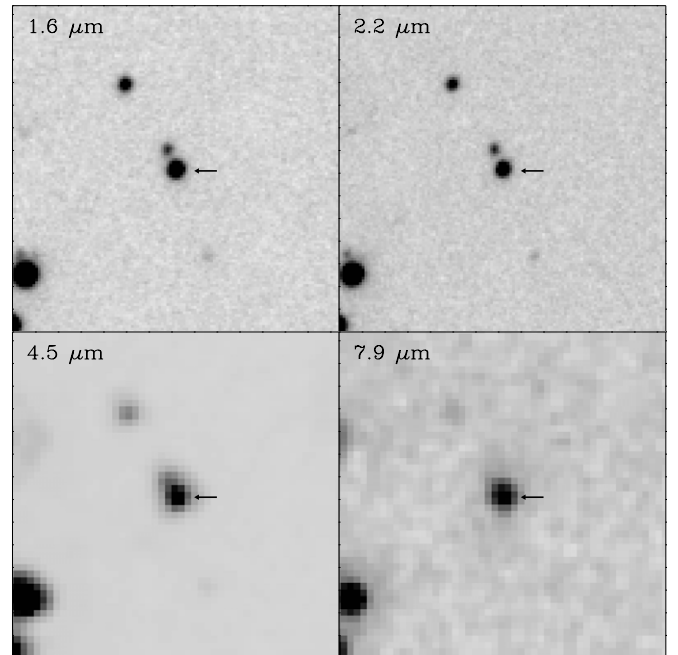| WD	J (mag)	H (mag)	K (mag)	Instrument
0110−565	16.23 ± 0.05	16.27 ± 0.05	16.24 ± 0.05	SOFI
0435+410	15.24 ± 0.05	15.16 ± 0.05	15.12 ± 0.05	LIRIS
0446−255	17.06 ± 0.05	17.09 ± 0.05	17.15 ± 0.05	SOFI
0449−259	16.52 ± 0.05	16.56 ± 0.05	16.60 ± 0.05	SOFI
0802+386	15.60 ± 0.05	15.59 ± 0.05	15.65 ± 0.05	LIRIS
0838+375	18.03 ± 0.05	18.02 ± 0.05	17.98 ± 0.05	LIRIS
0953+594	18.33 ± 0.06	18.29 ± 0.06	18.23 ± 0.06	WFCAM[a]
1015+377	17.24 ± 0.10	17.31 ± 0.12	16.78 ± 0.31	GEMINI[b]
1349−230	16.91 ± 0.05	16.94 ± 0.05	16.78 ± 0.05	SOFI
1350−162	17.13 ± 0.05	17.17 ± 0.05	17.25 ± 0.05	SOFI
1352+004	16.10 ± 0.05	16.12 ± 0.05	16.15 ± 0.05	LIRIS
1614+160	15.93 ± 0.05	15.97 ± 0.05	16.04 ± 0.05	SOFI
2229+139	16.29 ± 0.05	16.36 ± 0.05	16.53 ± 0.05	SOFI
2322+118	15.99 ± 0.05	15.98 ± 0.05	16.03 ± 0.05	SOFI

Notes.
[a] Obtained by one of us at UKIRT using WFCAM (Casali et al. 2007).
[b] Obtained by C. Melis at Lick Observatory with the GEMINI camera (McLean et al. 1993).

Figure 2. Infrared images of GD 61 taken with LIRIS at H and K_s, and *Spitzer* IRAC at 4.5 and 7.9 μm. All images are oriented north up and east left, and are $30''$ across, with $0\overset{''}{.}25$ pixel^{-1} for LIRIS and $0\overset{''}{.}6$ pixel^{-1} for IRAC. The white dwarf (marked by the arrow) is separated from a neighboring source by $1\overset{''}{.}9$. The neighbor does not influence the flux measurements presented in Table 3 (Section 3.1). The neighboring source must be in the background as its brightness never exceeds that of the white dwarf.

Figures 2 and 3 for the images of GD 61 and HE 1349−2305, respectively). The background object near GD 61 is separated by $1\overset{''}{.}9$ at P.A. $25°$ in the images taken with LIRIS (epoch 2011.2), and is readily resolved in the H and K bands. The near-infrared brightness of this neighbor is $(J, H, K) = (17.7, 17.0, 16.7)$ mag and never approaches the apparent magnitude of the white dwarf. Based on this fact and the colors of the neighbor, it must be a background object. This source contributes weakly in the 4.5 μm image, where it is well separated by APEX, and is no longer seen at 7.9 μm. CBS 127 and HE 1349−2305 both have neighbors $2\overset{''}{.}8$ distant (north and west, respectively); these are satisfactorily separated by PSF fitting with APEX.

3.2. Spectral Energy Distributions

Figures 4–7 illustrate the spectral energy distributions (SEDs) of the 15 metal-rich white dwarfs listed in Table 1. In addition to the supplementary near-infrared photometry described above, we include shorter wavelength photometry from a variety of literature and catalog sources (e.g., *GALEX*; Martin et al. 2005, SDSS DR7; Abazajian et al. 2009, DENIS; Epchtein et al.

1999, and CMC; Copenhagen University Obs. et al. 2006). In cases where independent *JHK* observations were not taken for this program, data from 2MASS (Skrutskie et al. 2006) and UKIDSS (Lawrence et al. 2007) were used. Where possible, a comparison of the IRAC photometry was made to data available at similar wavelengths from the *Wide-field Infrared Survey Explorer* (*WISE*; Wright et al. 2010).

For flux scaling of the spectral models in the figures, the most reliable photometry was used, which was primarily SDSS *ugriz* and the *JHK* data taken specifically for this program. Specifically, the *GALEX* fluxes were not used to constrain the white dwarf atmospheric models because (1) metal lines may significantly suppress these fluxes compared with a pure
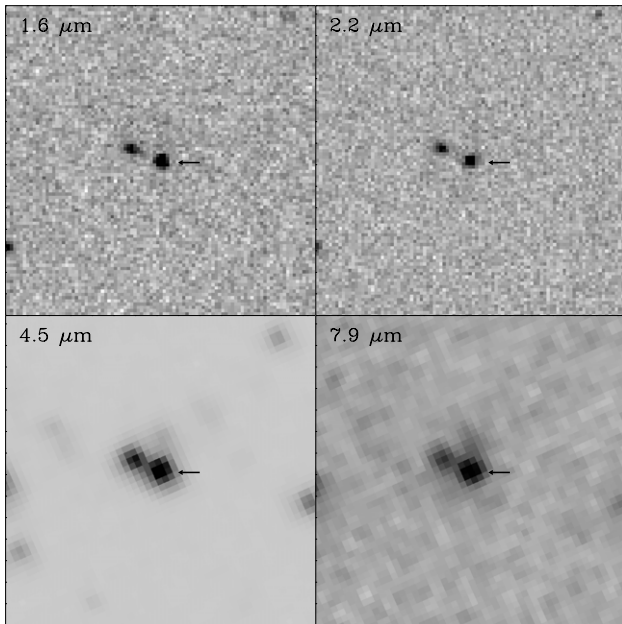
Figure 3. Infrared images of HE 1349−2305 taken with SOFI at *H* and *K*, and *Spitzer* IRAC at 4.5 and 7.9 μm. All images are oriented north up and east left, and are 30″ across, with 0″.25 pixel^{-1} for LIRIS and 0″.6 pixel^{-1} for IRAC. The white dwarf (marked by the arrow) is separated from a neighboring source by 2″.8, but does not influence the flux measurements presented in Table 3 (Section 3.1). The neighbor is clearly extended in the *H*-band image and is therefore extragalactic.

helium (or hydrogen) model atmosphere and (2) the interstellar reddening to these objects is not well known.

Table 1 lists the best available stellar parameters from the literature for each of the science targets. We used these parameters as an initial estimate for the white dwarf spectral models. A grid of synthetic white dwarf atmospheric spectra from Koester (2010) was interpolated to these temperature and surface gravity estimates. After comparing the fluxes from the models with the most reliable optical and near-infrared data, in some cases we found that a slightly different effective temperature provided a superior fit to the data (shown in the upper right corner of the relevant figure). These parameters thus used in the SED fits do not reflect an independent parameter determination, but rather our attempt to best constrain the infrared photospheric emission.

3.3. Stars with an Infrared Excess

We model stars with an infrared excess as a combination of the white dwarf photosphere and an optically thick, geometrically thin disk with a temperature profile $T_{\rm disk} \propto r^\beta$, with $\beta = -3/4$ (Adams et al. 1988; Chiang & Goldreich 1997; Jura 2003). The ratio of stellar radius to distance sets the absolute scale of the white dwarf photospheric flux, and is fixed in our modeling based on the best available parameters. The free parameters in the disk model are the inner disk radius ($R_{\rm in}$), the outer disk radius ($R_{\rm out}$) and the disk inclination (i). A grid of disk models was calculated with inner ($T_{\rm in}$) and outer disk temperatures ($T_{\rm out}$; each corresponding to a value of $R_{\rm in}$ and $R_{\rm out}$) ranging from 100 to 1800 K in steps of 50 K, and inclination ranging from 0 to 90° in steps of 5°. $T_{\rm out}$ was also fixed to be cooler than $T_{\rm in}$. A least χ^2 method was used to fit the *H*-, *K*-, and IRAC-band infrared fluxes and provide an estimate of the uncertainties.

In Figure 5, the panels show a slice through the χ^2 cube at the best-fit solution. The upper panel of each pair displays a slice
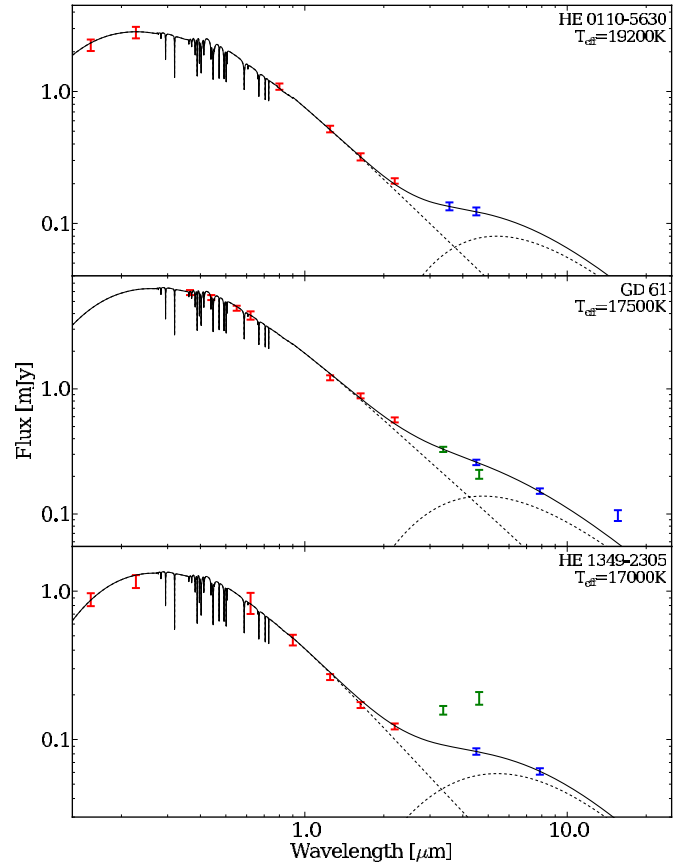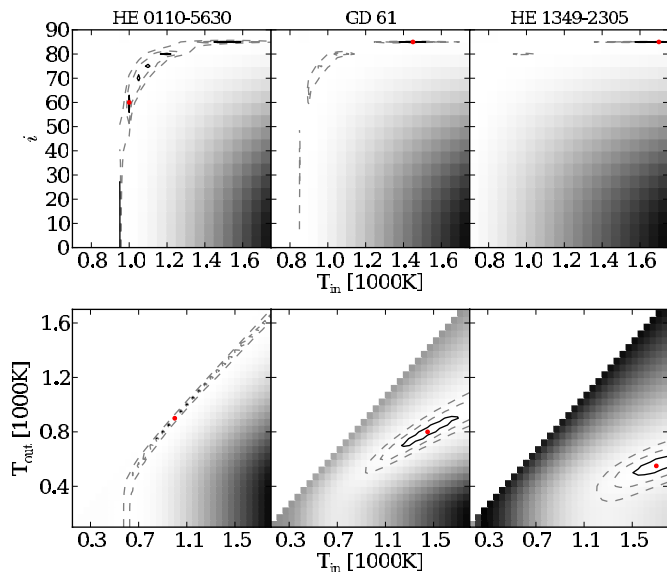

Figure 4. SED of HE 0110-5630, GD 61, and HE 1349−2305. The short-wavelength fluxes are: HE 0110-5630: *GALEX*, DENIS *I*-band, and SOFI *JHK*; GD 61: *UBV* (Eggen 1968), CMC *r'*, and LIRIS *JHK*; and HE 1349−2305: *GALEX*, CMC *r'*, DENIS *I*, and SOFI *JHK*. These are shown in red with error bars. *WISE* data are shown in green, however, they are clearly contaminated by the neighboring source for HE 1349−2305 (Section 3.1). The IRAC and IRS fluxes are shown in blue. The short-wavelength photometry is fitted with a stellar model that is displayed as a black dashed line. The minimum χ^2 disk model fit, shown in Figure 5, is displayed as a black dashed line, and the sum of the two is shown in solid black.

(A color version of this figure is available in the online journal.)

at the best-fitting $T_{\rm out}$, whilst the best-fit inclination defines the slice in the lower panel. Regions of high χ^2 are shown as dark areas and the least χ^2 solution is marked as a red circle and its flux is displayed in Figure 4. Solid black lines show the 1σ contours around the minimum, while 2σ and 3σ contours are shown as dashed gray lines. The upper left of each lower panel is excluded by the condition $T_{\rm in} > T_{\rm out}$.

The flat disk models naturally possess a modest degree of uncertainty. The three free parameters ($T_{\rm in}$, $T_{\rm out}$, and i) are somewhat degenerate in how they combine to determine the viewed solid angle of the disk. Even in the case when longer wavelength data (such as 24 μm photometry) are available, this degeneracy is not broken (Jura et al. 2007). Broadly speaking, the inner disk edges are fairly well constrained by their 2.2 and 3.6 μm emission. The 4.5 to 7.9 μm flux, however, can be reproduced by a relatively wide temperature range and a higher inclination, or a narrower temperature range and a lower inclination. Importantly, the newly detected disks mimic the emission seen at more than one dozen dusty white dwarfs observed with *Spitzer* IRAC and MIPS (e.g., Farihi et al. 2009) whose outer disk radii are consistently within the Roche limit of $d \gtrsim 1$ km solid bodies ($\sim 1\,R_\odot$). This corresponds to an outer disk temperature near 500 K, which is a likely lower limit for

Figure 5. Disk modeling for HE 0110-5630, GD 61, and HE 1349−2305. The infrared excess was fitted as described in Section 3.3. Briefly describing the format of the panels (see Section 3.3), a slice through the χ^2 volume is displayed each of the pairs of upper and lower panels for the minimum χ^2 fit. The upper panel shows a slice at the best-fitting $T_{\rm out}$ and the lower panel is defined by the best i. The best-fitting solutions are: HE 0110-5630: $T_{\rm in}$ = 1000 K, $T_{\rm out}$ = 900 K, i = 60°; GD 61: $T_{\rm in}$ = 1450 K, $T_{\rm out}$ = 800 K, i = 85°; and HE 1349−2305: $T_{\rm in}$ = 1700 K, $T_{\rm out}$ = 550 K, i = 85°. Regions of high χ^2 are shown as dark areas and the least χ^2 solution is marked by a red circle. Solid black lines show the 1σ contours around the minimum, while the 2σ and 3σ contours are shown as dashed gray lines. Because only slices through the χ^2 are shown, this does not show the full extent of the χ^2 surface. In the case of HE 0110-5630, i vs. $T_{\rm in}$, each of the regions enclosed by a solid black line represents a parameter space where χ^2 is within 1σ of the minimum. The χ^2 method does not constrain the disk parameters very well for HE 0110-5630.

(A color version of this figure is available in the online journal.)

$T_{\rm out}$ when interpreting the χ^2 surfaces. All together, the infrared emissions are precisely that expected for dust particles resulting from the tidal destruction of a large planetary body, whose constituent elements now rain onto and pollute the surfaces of the host stars.

HE 0110−5630. The available photometry for HE 0110−5630 consists of *GALEX* far- and near-UV, DE-NIS *I*-band, and *J*, *H*, and *K* measurements taken with SOFI. The photospheric emission is relatively well constrained by the *J*- and *H*-band fluxes and, therefore, so is the extrapolation to longer infrared wavelengths. The measured IRAC excess for HE 0110−5630 is consistent with warm circumstellar dust and is shown in Figure 4. The best-fit disk model has inner and outer temperatures of 1000 and 900 K, respectively, at an inclination of i = 60°. This corresponds to a narrow ring; however, as can be seen in the χ^2 panels, the solution is degenerate with respect to inner disk temperatures above 800 K, and inclination, and the outer temperature is not at all constrained. The χ^2 surfaces shown in Figure 5 show that a vast range in disk temperatures could provide a fit to the excess. We therefore cannot confidently estimate any of the disk parameters.

GD 61. From analysis of IRAC images and Peak-Up Imaging, this object was found to have an excess in Farihi et al. (2011). Here we include the *JHK* data taken with LIRIS to better constrain the stellar flux. These images resolve a nearby (background) source (Figure 2) that almost certainly contaminates the 2MASS photometry used in previous fits. From its spectral energy distribution and brightness, this object is not associated with the white dwarf. In the *Spitzer* IRAC

images, the PSF of the white dwarf and the contaminant overlap slightly; however, the APEX PSF-fitting photometry cleanly separates the two objects. We can therefore confirm the presence of a disk from the IRAC and IRS fluxes.

When performing χ^2 fitting of the infrared excess, we exclude the 15.6 μm flux due to a possible increase owing to silicate emission, and therefore the disk continuum emission would be overestimated. Such emission has been detected in all eight dusty white dwarfs observed spectroscopically with IRS (Reach et al. 2005; Jura et al. 2009). A disk model with inner- and outer-disk temperatures of 1450 and 800 K, respectively, and an inclination i = 85° is the best fit to the excess (Figures 4 and 5). The disk model temperature and inclination are again degenerate, and a large range of parameters would fit the infrared fluxes. We therefore find that the values reported previously ($T_{\rm in}$ = 1,300 K, $T_{\rm out}$ = 1,000 K and i = 79°; Farihi et al. 2011) are not inconsistent with ours, given the uncertainties in temperature and inclination.

HE 1349−2305. After deconvolving the white dwarf and neighboring background source (Section 3.1), a significant infrared excess is still found over the stellar model (Figure 4). The white dwarf photosphere is well constrained by short-wavelength and near-infrared photometry shown in Table 4. *WISE* 3.4 and 4.6 μm fluxes are also available for this object; however, the nearby source seen in Figure 3 is within the *WISE* beam width and therefore significantly contaminates the *WISE* fluxes. We therefore do not include these fluxes in the disk modeling. The excess is best fitted with a disk having $T_{\rm in}$ = 1,700 K, $T_{\rm out}$ = 550 K and an inclination of i = 85°. The uncertainties are rather modest in this case.

NLTT 51844. This was one of two white dwarfs bright enough for us to attempt blue Peak-Up image using IRS. The 15.6 μm flux measurement is in excess over the white dwarf model by slightly more than 3σ, similar to the MIPS 24 μm photometric excesses detected at G238-44 and G180-57 (Farihi et al. 2009). *Spitzer* galaxy counts at these wavelengths are 6×10^{-4} galaxies per square arcsecond (Marleau et al. 2004) for the brightness needed to produce an apparent excess in these cases. Therefore, the probability that such a source falls within a radius of two IRS Blue Peak-Up FWHM (3″.8) can be as high as 10%. Thus, the probability that three sources have excesses at roughly 20 μm (and not at shorter wavelengths) due to background objects, out of 30 stars surveyed at these longer wavelengths, can be as high as 65%.

While we cannot yet rule out a chance alignment in these cases, the astrometric position of NLTT 51844 in the IRS image mosaic coincides within 2″ of its position in the IRAC images based on the absolute *Spitzer* astrometry provided in the processed image files. Both NLTT 51844 and G180-57 are cool, helium-rich stars where metals can reside for Myr timescales, and hence their accretion history is unconstrained. In any case, dust that emits only at such long wavelengths must be sufficiently far from the white dwarf that it cannot be the immediate source of the atmospheric metals. Still, if the data for NLTT 51844 (as well as G238-44 and G180-57) are not spurious, we may be seeing an important clue to the nature of numerous polluted white dwarfs without obvious infrared excesses.

3.4. Stars without an Infrared Excess

The remaining white dwarfs (Figures 6 and 7) all show no evidence for infrared excess emission. They are relatively well constrained in the optical and near-infrared and therefore we can
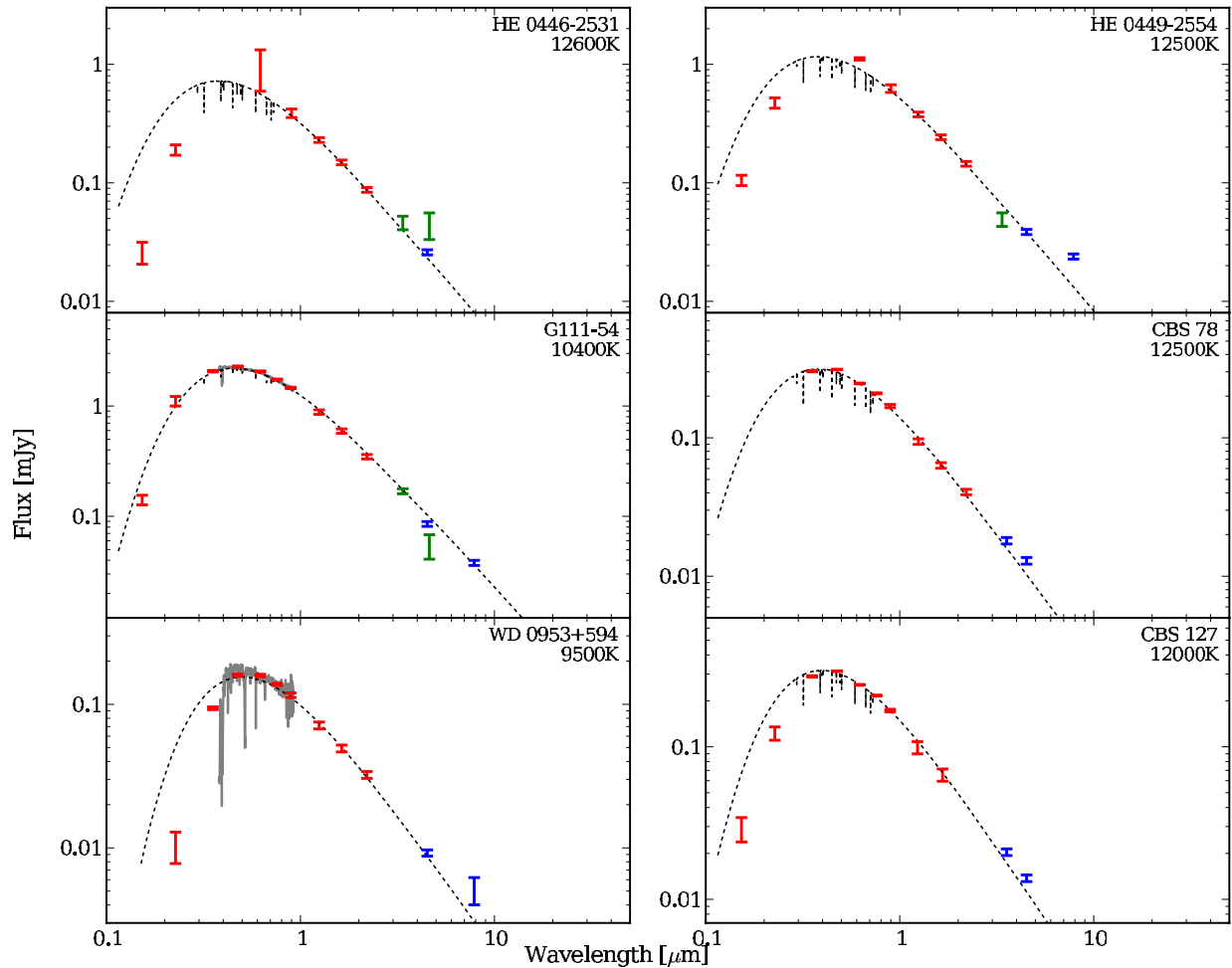
Figure 6. SEDs of 6 of the 12 science targets consistent with photospheric emission (Section 3.4). The figures follow the same general format as Figure 4. The SDSS optical spectrum of WD 0953+954 is shown as a gray line. The infrared excess seen in the SED of HE 0449−2554 is caused by light from a background object.

(A color version of this figure is available in the online journal.)

extrapolate with some certainty to IRAC wavelengths. Below we provide notes on a few particular stars.

HE 0446−2531. This star is perhaps the most highly polluted white dwarf observed by *Spitzer* and yet does not have an infrared excess. If the analysis of Friedrich et al. (2000) is correct, this star contains 8×10^{24} g of metals in its atmosphere—a mass approaching that of Pluto. The long diffusion timescale for heavy elements in this star allows for the possibility that a disk has been fully dissipated, but the very large mass involved suggests we are still within at most a few diffusion timescales of the accretion event. Two possibilities are: (1) accretion is ongoing from gaseous debris, or (2) accretion has ended but total mass involved was at least an order of magnitude higher. It is noteworthy that this star and HS 2253+8023 are both highly polluted (Friedrich et al. 2000) yet lack infrared excess, with HE 0446−2531 having nearly ten times more metal mass in its convection zone. However, Klein et al. (2011) found that HS 2253+8023 has an order of magnitude less calcium than originally reported by Friedrich et al. (2000), and therefore the same may be true of HE 0446−2531.

HE 0449−2554. A partly resolved extension is seen in the IRAC 7.9 μm image, and the combined source is offset slightly from the position of the white dwarf in the 4.5 μm image. While the SOFI *JHK* images of this star do not reveal any sources within a few arcseconds of the science target, the marginal,

apparent excess seen in the SED (Figure 6) is probably caused by a background object. Better data are needed to rule out contamination in IRAC.

CBS 127. As mentioned above, a background object lies within a few arcseconds of the white dwarf, and could potentially contaminate moderate-size apertures used for IRAC photometry. We used PSF-fitting routines within APEX to ensure both stars were photometrically disentangled. There is no infrared excess at this white dwarf.

HE 1350−1612 was observed in both the Cycle 5 and 6 programs and images were thus taken at 3.6, 4.5 (twice), and 7.9 μm. The average 4.5 μm flux is shown in Table 1 and Figure 7. The white dwarf was not detected in the 7.9 μm image, and thus a 3σ upper limit is given. Nevertheless, all infrared data are consistent with the predicted white dwarf photosphere.

PHL 131 is a 40,000 K white dwarf with interstellar calcium absorption, and hence not metal-rich. We do not analyze this star but its IRAC fluxes are reported in Table 3.

4. DISCUSSION

4.1. Updated Statistics and Accretion Rates

Of the 15 metal-polluted stars surveyed, three have an infrared excess consistent with circumstellar dust disk, and indicative of
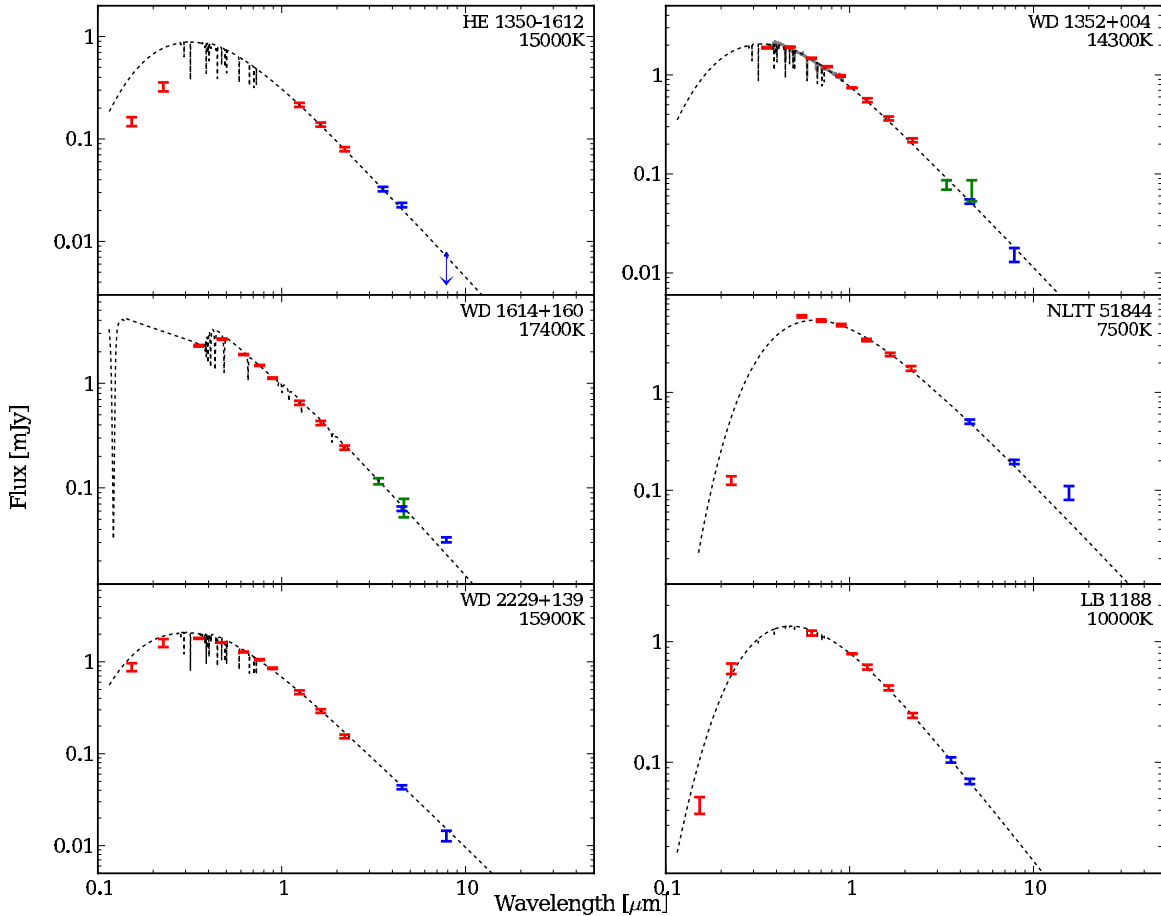
Figure 7. Continuation of Figure 6 for the remaining 6 of the 12 science targets consistent with photospheric emission (Section 3.4).
(A color version of this figure is available in the online journal.)

a remnant planetary system. Including the objects presented here, the total number of metal-polluted white dwarfs observed with *Spitzer* in Cycles 1 through 7 is 92. This includes the 52 objects from Table 4 of Farihi et al. (2009), 8 from Table 1 of Farihi et al. (2010b), 3 white dwarfs with gas disks from Gänsicke et al. (2006, 2007, 2008), 14 DBZ white dwarfs from Xu & Jura (2012), and the 15 objects studied here. Of these 92 objects, DAZ- and DBZ-type white dwarfs are represented in proportions of 39 and 53, respectively.

Our expanded study corroborates the previous finding (Kilic et al. 2008; Farihi et al. 2009, 2010b) that the detection of infrared excess is less frequent among DBZ white dwarfs than among their DAZ counterparts. 11 of 37 (30%) surveyed DAZ stars have circumstellar dust, whereas the same fraction for surveyed DBZ-type white dwarfs is only 7 of 52 (13%).[7] Because one would not expect disks to preferentially form around stars based on their atmospheric properties, the difference must be due to the longer diffusion timescales (Paquette et al. 1986; Koester & Wilken 2006). We will return to this point in more detail below.

Figure 8 illustrates the time-averaged metal accretion rate versus cooling age for the 88 metal-rich white dwarfs now observed by *Spitzer* with published abundances (four of the
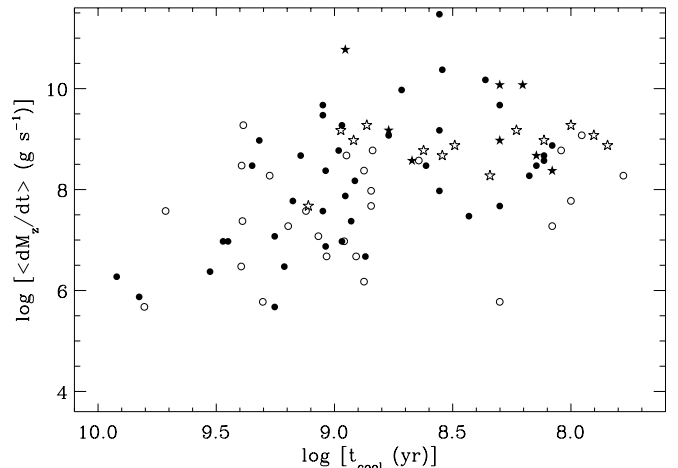
Figure 8. Time-averaged dust accretion rates vs. cooling age of the 88 metal-polluted white dwarfs, with published abundances, observed with *Spitzer* IRAC in Cycles 1 through 7. DAZ- and DBZ-type stars are plotted as open and filled circles, respectively, while objects with infrared excess are displayed as stars rather than circles.

Xu & Jura 2012 stars, including one with a detected infrared excess, do not have published abundances), updating Figure 10 from Farihi et al. (2010b). All accretion rates were calculated based on the accumulated metal abundances, using Equation 2 of Koester & Wilken (2006), as performed in Farihi et al. (2009). One difference between the method used in Farihi et al. (2009)

---

[7] We exclude here the two DAZ and one DBZ that were already known to have gaseous disks (Gänsicke et al. 2008) prior to their *Spitzer* observations. The stars discussed in Farihi et al. (2012) were also not included because they were observed with *Spitzer* after they were found to have an infrared excess in Girven et al. (2011).

and here is that in previous studies instantaneous and time-averaged accretion rates were calculated assuming the in-falling material either had solar calcium abundances (1 : 43; Koester & Wilken 2006), or 1% solar (1 : 109; i.e., metals only; Jura et al. 2007; Farihi et al. 2009) by mass fraction, based on the measured calcium abundance.

While the latter approach is still likely to be broadly correct, recent progress in the field enables a more accurate estimation. There are now of order 10 metal-polluted white dwarfs with measured Mg, Si, Ca, and Fe abundances (Zuckerman et al. 2003, 2007, 2010, 2011), and a handful also with O abundances (Dufour et al. 2010; Klein et al. 2010; Vennes et al. 2010; Klein et al. 2011; Melis et al. 2011; Vennes et al. 2011). Based on these data, it is increasingly clear that the accreted material has a composition similar to that of rocky, terrestrial material of the solar system. Zuckerman et al. (2010) find that Ca represents, on average, close to 1 part in 60, by mass, of all the accreted heavy elements. For comparison, this ratio is 1 part in 62.5 for the Earth (Allègre et al. 1995). Based on these facts, Figure 8 and Table 1 employ accretion rates and convective envelope masses, assuming Ca is 1.6% (1/62.5) of the total mass. To convert between the accretion rates quoted in Farihi et al. (2009, 2010b) and those shown in Figure 8, one must multiply by a factor of 109/62.5 for DAZ white dwarfs and 43/62.5 for DBZ white dwarfs.

Compared to the same figures shown in previous (related) papers, the accretion rates for the DAZ white dwarfs are therefore slightly decreased, while their DBZ counterparts are slightly increased.

### 4.2. A Simple Estimate of the Disk Lifetime

The mass of metals in the convective envelope of DBZ-type white dwarfs provides a lower limit on the total mass of the destroyed parent body. From the DAZ stars, we can infer the instantaneous accretion rates because one can safely assume accretion-diffusion equilibrium. There is no a priori reason that disks around hydrogen and helium-rich stars should be different (Jura et al. 2007). Therefore, assuming the inferred accretion rates of DAZ stars represent an accurate cross section over disk lifetimes, and similarly for the observed metal masses contained within DBZ stellar envelopes, we can obtain a typical disk lifetime by combining the average of these two observed quantities, i.e.,

$$t_{\rm disk} \sim \frac{\langle M_z \rangle_{\rm DBZ,disk}}{\langle dM_z/dt \rangle_{\rm DAZ,disk}}. \qquad (1)$$

Figure 9 demonstrates that the mass of metals in the convective envelope of DBZ white dwarfs is not a strong function of temperature, and hence cooling age. Therefore, calculating the average convective envelope metal mass across cooling ages should be robust. In contrast, the convective envelope depth increases substantially in this temperature range for DAZ stars (Koester 2009), as can be seen by the large increase in convective envelope metal masses at longer cooling ages in Figure 9.

Among 13 DAZ white dwarfs observed to have infrared excess with *Spitzer*, the average metal accretion rate is 9.7×10^8 g s^{-1}. Among eight DBZ-type stars with dust detected by *Spitzer*[8], the average metal content of the convection zone is 4.1×10^{22} g, and we thus estimate $t_{\rm disk} \simeq 1.3 \times 10^6$ yr.

---

[8] This does not include SDSS J220934.84+122336.5, the DBZ star from Xu & Jura (2012) with an infrared excess, because no calcium abundances are published.
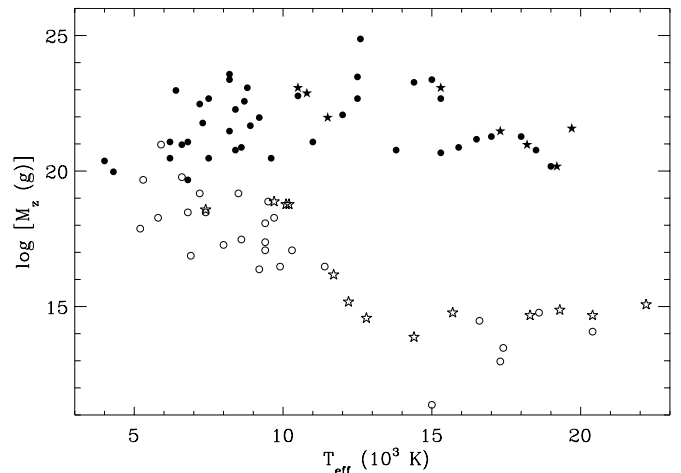
Figure 9. Mass of metals within the convective envelopes (or above $\tau = 5$, whichever is larger) of the 88 metal-polluted white dwarfs, with published abundances, observed with *Spitzer* IRAC in Cycles 1 through 7, plotted as a function of effective stellar temperature. DAZ- and DBZ-type stars are plotted as open and filled circles, respectively, while objects with infrared excess are displayed as stars rather than circles.

However, Figure 8 shows that the accretion rates and convection zone metal content vary by orders of magnitude, and suggests that using the logarithmic mean and standard deviation, $\langle \log[dM_z/dt \, ({\rm g \, s}^{-1})] \rangle = 8.8 \pm 0.4$ and $\langle \log[M_z \, ({\rm g})] \rangle = 21.9 \pm 1.1$, may be a more appropriate choice. The resulting estimate for the disk lifetime is $\log[t_{\rm disk} \, ({\rm yr})] = 5.6 \pm 1.1$. Because the metal masses in the DBZ stars are lower limits on the total parent body masses, it is reasonable to presume the same for the disk lifetimes.

At least 1% of all white dwarfs with cooling ages less than 0.5 Gyr have dusty disks (Farihi et al. 2009; Girven et al. 2011; Steele et al. 2011). Assuming that all white dwarfs host (remnants of) planetary systems and go through intermittent phases of debris, one would expect any given star to exhibit detectable infrared excess for $0.01 \times 0.5 \times 10^9$ yr $= 5 \times 10^6$ yr, which is broadly consistent with our estimate above.

4.3. How Complex is the Evolution of the Dust Disks?

Different possible scenarios for the evolution of dust disks, and corresponding estimates for their lifetimes have been discussed in more detail by Jura (2008), Rafikov (2011a, 2011b), and Bochkarev & Rafikov (2011).

A main motivation of the work of Jura (2008) was to explain the existence of metal-polluted white dwarfs without infrared excess detection by the continuous accretion from a gaseous disk that is replenished by the repeated tidal destruction of multiple small asteroids. In this scenario, dust disks are associated with the disruption of massive asteroids, and Jura (2008) estimated the lifetimes of the gaseous and dust disks to be $\sim 0.5 \times 10^4$ yr and $\sim 1.5 \times 10^5$ yr, respectively, though he underlined the uncertainty of these estimates. Jura (2008) discussed his scenario in the context of a much smaller sample of metal-polluted white dwarfs, in which the majority of high dM/dt stars were displaying infrared excess identifying the presence of dusty disks. It is unlikely that the much larger accretion rates that are now known for some stars without infrared excess can be explained by multiple impacts of small asteroids.

Rafikov (2011a) showed that Poynting–Robertson drag can explain accretion rates of $\sim 10^8$ g s^{-1}, and estimated the lifetime of massive ($\sim 10^{22}$ g) dust disks to several Myr. The higher

accretion rates observed in a number of white dwarfs require the presence of gas that increases the viscosity, and Rafikov (2011b) shows that sublimation of the inner disk may be sufficient to lead to a runaway evolution which produces accretion rates of 10^{10}–10^{11} g s^{-1}, exhausting the disk in $\sim 10^5$ yr. Rafikov (2011b) explicitly excluded the generation of gas by multiple impacts of additional asteroids. Extending the analysis to the global evolution of the debris disks, Bochkarev & Rafikov (2011) confirm that massive disks have expected life times of several Myr if subject to Poynting–Robertson drag only, but that sublimation may substantially shorten these estimates.

Our disk lifetime estimate in the previous section is broadly compatible with all the estimates summarized above. However, our approach assumed that accretion rates do not change significantly as a function of disk age, and that the *Spitzer* sample is representative of the potential changes in the accretion rate. Zuckerman et al. (2010) suggested that accretion onto a white dwarf could proceed through three distinct phases: a build-up, a steady state, and a decline, where the steady state lifetime should be orders of magnitude longer than the beginning and ending episodes. If correct, and disk lifetimes are typically $\simeq 10^6$ yr, then it will be very unlikely for an arbitrary white dwarf with circumstellar dust to be observed in anything other than a steady state phase.

Inspection of Figure 8 shows, as already mentioned in Section 4.1, that the fraction of DBZ with *Spitzer* infrared excess is substantially smaller than that of DAZ. The detection of dust seems to be associated with a minimum accretion rate, and if we only consider white dwarfs with $dM/dt \geqslant 10^8$ g s^{-1}, we find that 10/21 (48%) of DAZ have infrared excess, compared to only 7/30 (23%) for the DBZ.[9] This difference is, however, subject to small number statistics and future observations may show that both DAZ and DBZ are equally likely to show an infrared excess. If there is a real disparity, this fact is most likely related to the one significant difference between DBZ and DAZ—their diffusion timescales—and allows some independent gauge of the disk lifetime. Assuming a typical lifetime of the disks that is similar to or greater than the diffusion timescale of the DBZ stars ($t_{\rm disk} \gtrsim t_{\rm diff} \simeq 10^5 - 10^6$), we would expect a similar ratio of DAZ and DBZ stars exhibiting infrared excess. By contrast, if $t_{\rm disk} \ll t_{\rm diff}$, it would be very unlikely to detect the disks around any given DBZ. Thus, the small but non-negligible fraction of DBZ with observed infrared excess leads us to conclude that the typical disk lifetime is somewhat shorter than the diffusion timescales in DBZ—or that the disk lifetimes vary by substantial amounts (which is in fact consistent with the large uncertainty in our logarithmic estimate of the life time). It appears unlikely that a large fraction of the highly polluted DBZ white dwarfs without infrared excess are currently accreting from a gaseous disk, as the lifetimes of these gaseous disks are short (Jura 2008).

Figure 8 also reveals a fairly well defined upper limit in dM/dt for DAZ white dwarfs. Based on our updated calculation of the accretion rates, there are no DAZ white dwarfs observed with *Spitzer* with accretion rates above 2×10^9 g s^{-1}. The most extremely metal-polluted DAZ white dwarf star currently known, GALEX 1931+0117[10] (Vennes et al. 2010), still only accretes at a rate of 3–4×10^9 g s^{-1} (Melis et al. 2011; Vennes et al. 2011). In contrast, there are several DBZ white dwarfs with metal accretion rates one to two orders of magnitude larger than observed in any DAZ,

and substantially exceeding the rates that can be explained by Poynting–Robertson drag (Rafikov 2011a, 2011b). For instance, HE 0446–2531, HE 0449–2554, and HE 1350–162 all have accreted several 10^{23} g to nearly 10^{25} g within the last diffusion timescale, i.e., $\simeq 10^6$ yr (or correspondingly larger amounts of material if the accretion ended several diffusion timescales ago). This is comparable to the extremely metal-polluted DZ white dwarf, SDSS J0956+5912, which has at least 1.5×10^{23} g of metals in its atmosphere (Koester et al. 2011). Assuming the planetary bodies and physical mechanisms do not depend on the type of white dwarf, this substantial difference in the maximum accretion rates found for DAZ and DBZ white dwarfs forces us to conclude that either the calculated metal accretion rates for DBZ white dwarfs suffer from systematic errors, or the extremely high metal accretion rates found among DBZ white dwarfs simply have not been seen yet in DAZ white dwarfs.

One may speculate that both DAZ and DBZ white dwarfs can undergo a short-lived phase of very high rate accretion. Whereas the long diffusion timescales of DBZ provide an efficient "memory" to such events, the opposite is true for the DAZ, where the large amount of metals would be cleared out of the atmosphere within days to at most years—reducing the probability of witnessing such an event. A number of possible scenarios that would lead to such phases are conceivable. Secondary impacts of asteroids on an existing massive dust disk could generate sufficient amounts of gas to lead to runaway accretion (Jura 2008). Alternatively, a collisional cascade in the initially highly eccentric disk may generate sufficient amounts of gas to cause runaway accretion, effectively preventing the formation of a longer lived disk. In either scenario, the perturbed debris disks are expected to evolve on relatively short timescales, and Gänsicke et al. (2008) have shown that the structure of the gaseous disk in SDSS J084539.17+225728.0 changes on timescales of a few years. An initial spike in the accretion rate could also be related to the direct accretion of a substantial fraction of the disrupted asteroid, with the possible subsequent formation of a debris disk feeding the white dwarf at a lower rate. Another alternative comes from the fact that asteroid accretion events are, by definition, produced from eccentric orbits. One can therefore envisage that a fraction of disks are therefore born in an unstable configuration. The disk would, similarly to the above scenario, have many disk–disk interactions, producing a significant amount of gas. Therefore, the disk could accrete at a very high rate, leaving a heavily polluted white dwarf without a dust disk.

5. CONCLUSIONS

We obtained and analyzed *Spitzer* observations of 15 white dwarfs with metal-polluted atmospheres, all but one having helium-dominated atmospheres. Of these, HE 0110−5630, GD 61, and HE 1349−2305 are found to have an infrared excess consistent with closely orbiting circumstellar dust. These disks are likely formed from the disruption of large asteroid analogs within the remnant planetary systems. A marginal excess is measured at 15.6 μm around NLTT 51844, but more data are needed to rule out contamination from extragalactic sources.

This survey nearly doubles the number of disk detections around DBZ white dwarfs. Using this substantially enlarged sample, we estimate a typical disk lifetime by comparing the accreted metal masses inferred from DBZ stars with dust to the instantaneous accretion rates for DAZ stars with dust. Accounting for the large scatter by taking the logarithmic average, we find $\log[t_{\rm disk}({\rm yr})] = 5.6 \pm 1.1$, which is compatible

---

[9] Again excluding the two DAZ and one DBZ that were identified because of their gaseous discs (Gänsicke et al. 2008).

[10] Not included in our figure because it has not been observed with *Spitzer*.

with the relatively large range of disk lifetimes estimated from different theoretical models of white dwarf disks.

The fraction of highly polluted DBZ white dwarfs exhibiting an infrared excess is low (23%) compared to that among DAZ white dwarfs (48%). Assuming that the formation and evolution of circumstellar disks is similar for both types of stars, this difference suggests that the disk lifetimes are typically shorter than the DBZ diffusion timescales.

We also show that the highest time-averaged accretion rates are found among white dwarfs with helium-rich atmospheres, many of which do not exhibit infrared excess, and we suggest that these stars have experienced very high accretion rates during short-lived phases. These events should occur in hydrogen-dominated white dwarfs as well, but their short diffusion timescales substantially lower the probability of detection.

REFERENCES

Abazajian, K. N., Adelman-McCarthy, J. K., Agüeros, M. A., et al. 2009, ApJS, 182, 543
Adams, F. C., Shu, F. H., & Lada, C. J. 1988, ApJ, 326, 865
Allègre, C. J., Poirier, J., Humler, E., & Hofmann, A. W. 1995, Earth Planet. Sci. Lett., 134, 515
Bochkarev, K. V., & Rafikov, R. R. 2011, ApJ, 741, 36
Brinkworth, C. S., Gänsicke, B. T., Girven, J. M., et al. 2012, ApJ, in press (arXiv:1202.6411)
Brinkworth, C. S., Gänsicke, B. T., Marsh, T. R., Hoard, D. W., & Tappert, C. 2009, ApJ, 696, 1402
Casali, M., Adamson, A., Alves de Oliveira, C., et al. 2007, A&A, 467, 777
Chiang, E. I., & Goldreich, P. 1997, ApJ, 490, 368
Copenhagen University Obs., Institute of Astronomy, Cambridge, Univ., & Real Instituto y Observatorio de la Armada en San Fernando. 2006, Carlsberg Meridian Catalog Number 14
Davidsson, B. J. R. 1999, Icarus, 142, 525
Debes, J. H., Hoard, D. W., Kilic, M., et al. 2011, ApJ, 729, 4
Debes, J. H., & Sigurdsson, S. 2002, ApJ, 572, 556
Desharnais, S., Wesemael, F., Chayer, P., Kruk, J. W., & Saffer, R. A. 2008, ApJ, 672, 540
Dufour, P., Bergeron, P., Liebert, J., et al. 2007, ApJ, 663, 1291
Dufour, P., Kilic, M., Fontaine, G., et al. 2010, ApJ, 719, 803
Dupuis, J., Fontaine, G., Pelletier, C., & Wesemael, F. 1993, ApJS, 84, 73
Eggen, O. J. 1968, ApJS, 16, 97
Epchtein, N., Deul, E., Derriere, S., et al. 1999, A&A, 349, 236
Farihi, J., Barstow, M. A., Redfield, S., Dufour, P., & Hambly, N. C. 2010a, MNRAS, 404, 2123
Farihi, J., Brinkworth, C. S., Gänsicke, B. T., et al. 2011, ApJ, 728, L8
Farihi, J., Gänsicke, B. T., Steele, P. R., et al. 2012, MNRAS, 2359
Farihi, J., Jura, M., Lee, J., & Zuckerman, B. 2010b, ApJ, 714, 1386
Farihi, J., Jura, M., & Zuckerman, B. 2009, ApJ, 694, 805
Farihi, J., Zuckerman, B., & Becklin, E. E. 2008, ApJ, 674, 431
Fazio, G. G., Hora, J. L., Allen, L. E., et al. 2004, ApJS, 154, 10
Friedrich, S., Koester, D., Christlieb, N., Reimers, D., & Wisotzki, L. 2000, A&A, 363, 1040
Gänsicke, B. T., Koester, D., Marsh, T. R., Rebassa-Mansergas, A., & Southworth, J. 2008, MNRAS, 391, L103
Gänsicke, B. T., Marsh, T. R., & Southworth, J. 2007, MNRAS, 380, L35
Gänsicke, B. T., Marsh, T. R., Southworth, J., & Rebassa-Mansergas, A. 2006, Science, 314, 1908
Girven, J., Gänsicke, B. T., Steeghs, D., & Koester, D. 2011, MNRAS, 417, 1210
Graham, J. R., Matthews, K., Neugebauer, G., & Soifer, B. T. 1990, ApJ, 357, 216
Greenstein, J. L. 1956, Vistas Astron., 2, 1299
Hagen, H.-J., Groote, D., Engels, D., & Reimers, D. 1995, A&AS, 111, 195
Houck, J. R., Roellig, T. L., Van Cleve, J., et al. 2004, Proc. SPIE, 5487, 62
Hunt, L. K., Mannucci, F., Testi, L., et al. 1998, AJ, 115, 2594
Jura, M. 2003, ApJ, 584, L91
Jura, M. 2008, AJ, 135, 1785
Jura, M., Farihi, J., & Zuckerman, B. 2007, ApJ, 663, 1285
Jura, M., Farihi, J., & Zuckerman, B. 2009, AJ, 137, 3191
Kilic, M., Farihi, J., Nitta, A., & Leggett, S. K. 2008, AJ, 136, 111
Kilic, M., von Hippel, T., Leggett, S. K., & Winget, D. E. 2006, ApJ, 646, 474
Klein, B., Jura, M., Koester, D., & Zuckerman, B. 2011, ApJ, 741, 64
Klein, B., Jura, M., Koester, D., Zuckerman, B., & Melis, C. 2010, ApJ, 709, 950
Koester, D. 2009, A&A, 498, 517
Koester, D. 2010, Mem. Soc. Astron. Ital., 81, 921
Koester, D., Girven, J., Gänsicke, B. T., & Dufour, P. 2011, A&A, 530, A114
Koester, D., Napiwotzki, R., Voss, B., Homeier, D., & Reimers, D. 2005a, A&A, 439, 317
Koester, D., Rollenhagen, K., Napiwotzki, R., et al. 2005b, A&A, 432, 1025
Koester, D., & Wilken, D. 2006, A&A, 453, 1051
Lawrence, A., Warren, S. J., Almaini, O., et al. 2007, MNRAS, 379, 1599
Makovoz, D., Roby, T., Khan, I., & Booth, H. 2006, Proc. SPIE, 6274, 10
Manchado, A., Fuentes, F. J., Prada, F., et al. 1998, Proc. SPIE, 3354, 448
Marleau, F. R., Fadda, D., Storrie-Lombardi, L. J., et al. 2004, ApJS, 154, 66
Martin, D. C., Fanson, J., Schiminovich, D., et al. 2005, ApJ, 619, L1
McLean, I. S., Becklin, E. E., Brims, G., et al. 1993, SPIE, 1946, 513
Melis, C., Farihi, J., Dufour, P., et al. 2011, ApJ, 732, 90
Moorwood, A., Cuby, J.-G., & Lidman, C. 1998, The Messenger, 91, 9
Paquette, C., Pelletier, C., Fontaine, G., & Michaud, G. 1986, ApJS, 61, 177
Rafikov, R. R. 2011a, ApJ, 732, L3
Rafikov, R. R. 2011b, MNRAS, 416, L55
Reach, W. T., Kuchner, M. J., von Hippel, T., et al. 2005, ApJ, 635, L161
Reach, W. T., Lisse, C., von Hippel, T., & Mullally, F. 2009, ApJ, 693, 697
Sion, E. M., Leckenby, H. J., & Szkody, P. 1990, ApJ, 364, L41
Skrutskie, M. F., Cutri, R. M., Stiening, R., et al. 2006, AJ, 131, 1163
Steele, P. R., Burleigh, M. R., Dobbie, P. D., et al. 2011, MNRAS, 416, 2768
Subasavage, J. P., Henry, T. J., Bergeron, P., et al. 2007, AJ, 134, 252
van Maanen, A. 1917, PASP, 29, 258
Vennes, S., Kawka, A., & Németh, P. 2010, MNRAS, 404, L40
Vennes, S., Kawka, A., & Németh, P. 2011, MNRAS, 413, 2545
von Hippel, T., Kuchner, M. J., Kilic, M., Mullally, F., & Reach, W. T. 2007, ApJ, 662, 544
Voss, B., Koester, D., Napiwotzki, R., Christlieb, N., & Reimers, D. 2007, A&A, 470, 1079
Weidemann, V. 1960, ApJ, 131, 638
Wisotzki, L., Koehler, T., Groote, D., & Reimers, D. 1996, A&AS, 115, 227
Wright, E. L., Eisenhardt, P. R. M., Mainzer, A. K., et al. 2010, AJ, 140, 1868
Xu, S., & Jura, M. 2012, ApJ, 745, 88
Zuckerman, B., & Becklin, E. E. 1987, Nature, 330, 138
Zuckerman, B., Koester, D., Dufour, P., et al. 2011, ApJ, 739, 101
Zuckerman, B., Koester, D., Melis, C., Hansen, B. M., & Jura, M. 2007, ApJ, 671, 872
Zuckerman, B., Koester, D., Reid, I. N., & Hünsch, M. 2003, ApJ, 596, 477
Zuckerman, B., Melis, C., Klein, B., Koester, D., & Jura, M. 2010, ApJ, 722, 725